Synthesis and Implementation of Multiband SIW Bandpass Filters Based on In-Line Topology

Yu Zhan, Yi Wu, Erwan Fourn, Philippe Besnier, Kaixue Ma

Synthesis and Implementation of Multiband SIW Bandpass Filters Based on In-Line Topology

Yu Zhan, *Student Member, IEEE*, Yi Wu, *Member, IEEE*, Erwan Fourn, *Member, IEEE*, Philippe Besnier, *Senior Member, IEEE*, and Kaixue Ma, *Fellow, IEEE*

***Abstract*— This article presents a similarity transformation method for multiband bandpass filters (MBPFs) to convert the star-like topology into the in-line topology. A general theoretical technique is introduced, which replaces the traditional step-by-step extraction of *LC* circuit through filter synthesis with the similarity transformation rotation of coupling matrix, addresses the round-off errors in the parameter extraction process, and improves the accuracy of the theoretical synthesis results. The application of in-line topology significantly enhances the flexibility of filter design, reduces circuit complexity, and simplifies the fabrication of high-order MBPFs. Based on the substrate integrated waveguide (SIW) technology, a series of examples, including tri-band, quad-band, and particularly the first reported quint-band third-order Chebyshev SIW bandpass filters, is designed and implemented. Good agreement is achieved between simulated responses and measured results, validating the designed filter models and the proposed theoretical method.**

***Index Terms*— Coupling matrix rotation, in-line topology, multiband bandpass filter (MBPF), similarity transformation method, substrate integrated waveguide (SIW).**

I. Introduction

THE widespread adoption of 5G technology has further exacerbated the scarcity of spectrum resources, making efficient spectrum resource utilization imperative. Fig. 1 shows the typical architecture of an RF front-end module with multiband bandpass filters (MBPFs). As critical components of RF front-end systems, MBPFs play a crucial role in enabling effective coexistence and simultaneous operation of multiple wireless services, providing essential hardware support for mainstream communication technologies, such as multichannel transmission, frequency-division multiple access (FDMA), and time-division multiple access (TDMA).

In addition, the application of MBPFs holds significant importance in enhancing system integration and anti-interference capabilities, improving spectrum efficiency, and expanding system capacity. Consequently, it becomes pivotal for ensuring efficient and reliable wireless communication in the era of 5G and beyond.

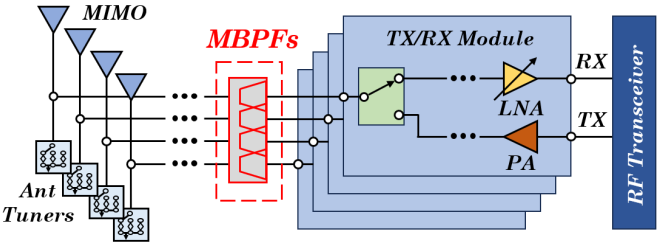

Fig. 1. Typical architecture of an RF front-end module with MBPFs.

Recently, because of its high Q-factor, high power capacity, low cost, and high integration, the substrate integrated waveguide (SIW) technology has been widely applied in the design of various RF modules, such as antenna arrays, filters, power dividers, couplers, and power amplifiers [1], [2], [3], [4], [5], [6], [7], [8], [9], [10], [11], [12], [13]. Among them, approaches for achieving MBPFs received widespread attention and reports from scholars. Summarizing related research, the common methods of SIW MBPFs outlined are as follows.

1) *Multimode Design [14], [15], [16], [17], [18], [19], [20], [21]:* This method utilizes multimode resonators for the design of MBPFs. However, due to the frequency correlations among multiple modes, it is exceedingly difficult to render the accurate and independent control of each resonant frequency, which greatly constrains the flexibility and versatility of frequency design specification. Furthermore, there exist complex coupling relationships between multiple modes, which cannot be precisely controlled. This limitation significantly heightens the complexity of multimode resonator design, resulting in intricate and challenging simulation and optimization of MBPFs.
2) *Multilayer or 3-D Design [22], [23], [24], [25], [26]:* This approach involves the vertical or 3-D stacking of multiple filter layers. However, it requires careful consideration of factors such as coupling, routing, and interconnections between adjacent layers during the design process. Precise control of alignment and gaps between layers is necessary during assembly. As a result, this method greatly increases the complexity of circuit design and assembly, introduces additional circuit losses, and escalates manufacturing risks.

Manuscript received 25 January 2024; revised 26 March 2024 and 19 April 2024; accepted 21 April 2024. This work was supported in part by the Natural Science Foundation of China under Grant 62301358 and Grant 62341409, and in part by the Research Program under Grant 22JCQNJC00570. *(Corresponding author: Yi Wu.)*

Yu Zhan, Yi Wu, and Kaixue Ma are with the School of Microelectronics, Tianjin University, Tianjin 300072, China (e-mail: Tjusmezy@gmail.com; wuyiciomp@gmail.com; makaixue@tju.edu.cn).

Erwan Fourn and Philippe Besnier are with CNRS, Institut d'Electronique et des Technologies du numéRique (IETR)-UMR 6164, Institut National des Sciences Appliquées de Rennes (INSA-Rennes), 35000 Rennes, France (e-mail: Erwan.Fourn@insa-rennes.fr; philippe.besnier@insa-rennes.fr).

Color versions of one or more figures in this article are available at https://doi.org/10.1109/TMTT.2024.3392890.

Digital Object Identifier 10.1109/TMTT.2024.3392890

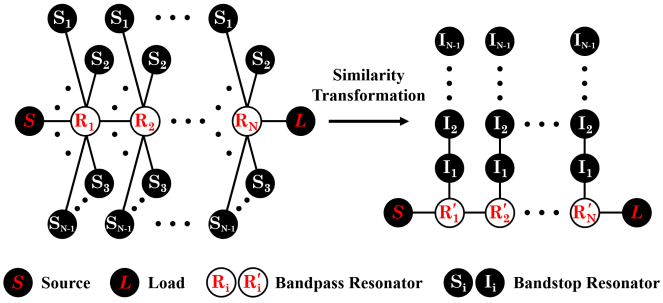

Fig. 2. Similarity transformation from star-like topology to in-line topology.

3) *Stacked Resonators [27], [28], [29], [30]:* This method involves using a stack of resonators, such as star-like or parallel topology. However, the compact spatial layout of the resonators requires higher precision in circuit manufacturing. Furthermore, the presence of multiple adjacent resonators increases coupling and interaction between resonators, leading to undesirable frequency shifting and distortion.

During the parameter extraction process in filter synthesis, round-off errors are typically introduced. Especially when dealing with high-order polynomials, these errors will accumulate step by step and ultimately affect the accuracy of the theoretical synthesis results. This article presents a similarity transformation method for MBPF design, as shown in Fig. 2, which converts the star-like topology into the in-line topology to solve the round-off errors issue. The main contributions of this article can be summarized as follows.

1) In theory, a general technique to convert the star-like topology into in-line topology based on similarity transformation of coupling matrix is proposed, which solves the round-off errors in the process of parameter extraction for capacitance and inductance of bandpass and bandstop resonators, leading to more accurate results.
2) In design, the proposed method allows for flexible control over theoretical frequency response, mainly including passband number, filter order, frequency spacing ratio, and bandwidth, providing a highly accurate coupling matrix. The application of periodic resonator cells greatly simplifies the design of high-order MBPFs.
3) In mechanism, unlike the multimode, which is hard to simultaneously control, the resonant frequencies of in-line resonator cell can be precisely regulated by adjusting the physical size of each cavity and the coupling strength between resonators, effectively simplifying the design and optimization of MBPFs.
4) In implementation, for the in-line topology rotated from the star-like topology, the coupling coefficients increase significantly, which in turn increases the size of coupling windows, reducing processing difficulty and improving the manufacturing tolerance of high-order MBPFs.

We substantiate the practicality and universality of our proposed similarity transformation method by conducting a comprehensive process encompassing filter synthesis—theoretical verification, model simulation, and experimental measurement. Three examples of third-order Chebyshev MBPFs (tri-, quad-, and quint-bands) are fabricated and measured. The comparison between the simulated responses and measured results reveals a satisfactory level of agreement.

II. Theoretical Derivation of Similarity Transformation Method

The proposed similarity transformation method starts with a frequency mapping function, which enables the synthesis of compound resonators that replace the single resonators of an original single-band prototype. The prototype can be symmetric or asymmetric, with or without cross-couplings, and the multiband prototype can accommodate, in principle, an unrestricted number of subbands with independently prescribed bandwidths. The bands of MBPFs become the bandwidth-scaled and frequency-translated copies of the initial prototype. The frequency mapping function is a rational polynomial equation as

$$\Omega^{(N)}(\omega) = \frac{\omega^N + n_{N-1}\omega^{N-1} + n_{N-2}\omega^{N-2} \cdots + n_0}{m_{N-1}\omega^{N-1} + m_{N-2}\omega^{N-2} \cdots + m_0} \tag{1}$$

where N is the number of bands. The numerator polynomial is of degree N, and the denominator is of degree $N-1$. ω is the frequency in the denormalized multiband domain, and Ω is the corresponding frequency in the normalized low-pass domain.

For the star-like topology, we may rewrite $\Omega^{(N)}(\omega)$ in the form of fraction, which consists of two polynomials, $n(\omega)$ and $m(\omega)$, with degrees N and $N-1$, respectively, and further decompose it into the sum of several simple fractions, written as follows:

$$\begin{aligned}\Omega^{(N)}(\omega) &= \frac{n(\omega)}{m(\omega)} \\ &= A\omega + B + \frac{r_1}{\omega - k_1} + \cdots + \frac{r_{N-1}}{\omega - k_{N-1}}.\end{aligned} \tag{2}$$

This sum is the partial fraction expansion of $\Omega^{(N)}(\omega)$. A and B are constant; $r_1, \ldots, r_N$ are the residues; and $k_1, \ldots, k_{N-1}$ are the zeros of function (2).

For generalized frequency transformation with star-like topology, the mapping function (1) could be described by a multiband resonator (MR) with LC circuits. Each MR can produce $N-1$ transmission zeros (TZs) and N reflection zeros (poles), which can be expressed in a low-pass domain

$$\begin{aligned}\Omega^{(N)}(\omega) = \omega C_{L0} + B_{L0} - \frac{1}{\omega C_{L1} + B_{L1}} - \frac{1}{\omega C_{L2} + B_{L2}} \\ - \cdots - \frac{1}{\omega C_{L(N-1)} + B_{L(N-1)}}.\end{aligned} \tag{3}$$

By comparing (2) and (3), we can immediately construct the correlation between the mathematical model and the low-pass domain and obtain the following relationship:

$$C_{L0} = k_1 \tag{4a}$$

$$B_{L0} = k_2 \tag{4b}$$

$$C_{Li} = -\frac{1}{r_i} \tag{4c}$$

$$B_{Li} = \frac{k_i}{r_i} = -k_i C_i. \tag{4d}$$

Defining the fractional bandwidth as FBW, the slope parameter and the resonant frequency of resonator can be written as

$$b_k = \frac{C_{Lk}}{\mathrm{FBW}} \tag{5}$$

$$\omega_k = \omega_{\mathrm{BP}}\left(-\frac{B_{Lk}\mathrm{FBW}}{2C_{Lk}} + \sqrt{\left(\frac{B_{Lk}\mathrm{FBW}}{2C_{Lk}}\right)^2 + 1}\right). \tag{6}$$

Thus, the coupling coefficients between bandpass resonators can be expressed as

$$k_{i,i+1} = \frac{\mathrm{FBW}}{C_0}\sqrt{\frac{1}{g_i g_{i+1}}}. \tag{7}$$

Also, the coupling coefficients between the bandpass resonator and the bandstop resonator can be written as

$$k_{s,s'} = \mathrm{FBW}\sqrt{\frac{-r_1}{C_0}}. \tag{8}$$

All the couplings between bandpass resonators are synchronously tuned, while all the couplings between bandstop resonators are asynchronously tuned. The couplings between bandpass resonators and bandstop resonators are also asynchronously tuned. In this type of topology, couplings exist between the bandpass resonator and $N-1$ bandstop resonators for N passbands MBPFs.

However, one drawback of the star-like configuration is that it imposes a higher load on the bandpass resonators, increasing the coupling and interaction between adjacent bandstop resonators, and finally leading to undesirable frequency shifting and distortion. Therefore, implementing MBPFs in cavity modes with a large number of bands in star-like topology is difficult. To overcome this challenge, it is helpful to transform the star-like topology into alternative coupling structures, so as to effectively address the issues associated with the filter topology and the coupling matrix. A common approach is to reduce the couplings through a series of similarity transformations and eliminate the specific elements in the coupling matrix, aiming to achieve a more convenient form with minimal couplings. In order to achieve an easily implementable topology, here we convert the star-like topology into the in-line topology using a series of matrix rotations. It should be noted that both star-like topology and in-line topology exhibit periodicity in structures. To facilitate the analysis, the overall MBPFs are divided into multiple repetitive resonator cells, and the number of resonator cells is equal to the filter order. In the subsequent analysis, the similarity transformation of filter topology and the calculation of coupling matrix will be carried out using a single resonator cell as the basis. Fig. 3 shows the schematic of the similarity transformation from star-like topology resonator cell to in-line topology resonator cell. As shown, in an N-band filter, each resonator cell contains N subresonators, which consists of one subresonator set at the center to provide poles, marked as R_1, and $N-1$ subresonators to provide TZs, marked as S_1 to S_{N-1} in star-like topology or I_1 to I_{N-1} in in-line topology. N-band filter has $N-1$ stopbands. In general, for the coupling matrix of the star-like topology, apart from the diagonal elements that indicate the self-coupling, the remaining elements are solely distributed in the first row and the first column, with all other

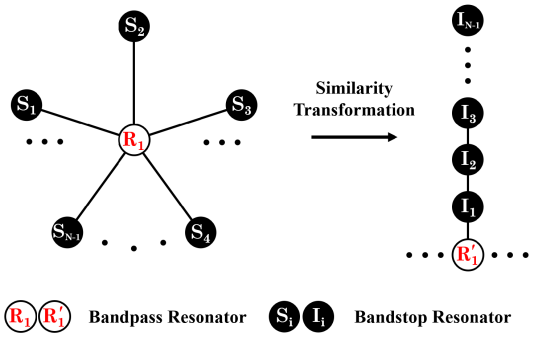

Fig. 3. Similarity transformation from star-like resonator cell to in-line resonator cell.

elements set to zero. Thus, the coupling matrix of the star-like resonator cell can be expressed as follows:

$$M_S^{(N)} = \begin{array}{c} \\ 1 \\ 2 \\ 3 \\ \vdots \\ N \end{array} \begin{array}{c} \begin{array}{ccccc} 1 & 2 & 3 & \cdots & N \end{array} \\ \begin{bmatrix} m_{11} & m_{12} & m_{13} & \cdots & m_{1N} \\ m_{21} & m_{22} & 0 & 0 & 0 \\ m_{31} & 0 & m_{33} & 0 & 0 \\ \vdots & \vdots & \vdots & \ddots & \vdots \\ m_{N1} & 0 & 0 & \cdots & m_{NN} \end{bmatrix} \end{array}. \tag{9}$$

To convert the coupling matrix from the star-like resonator cell to the in-line resonator cell, a similarity transformation method is applied to reduce the coupling and eliminate the specific elements inside the coupling matrix of star-like resonator cell. The coupling matrix M_I of in-line resonator cell can be obtained based on M_S, by pre-multiplying a rotation matrix R_r and post-multiplying its transpose R_r^T, as outlined in the following:

$$M_I^{(N)} = R_r M_S^{(N)} R_r^T \tag{10}$$

$$R_r = \begin{bmatrix} 1 & & & & \\ & \ddots & & & \\ & & R_{ii}(\cos\theta_r) & R_{ij}(-\sin\theta_r) & \\ & & \vdots & \vdots & \\ & & R_{ji}(\cos\theta_r) & R_{jj}(\sin\theta_r) & \\ & & & \ddots & \\ & & & & 1 \end{bmatrix} \tag{11}$$

$$M_I^{(N)} = \begin{array}{c} \\ 1 \\ 2 \\ 3 \\ \vdots \\ N \end{array} \begin{array}{c} \begin{array}{ccccc} 1 & 2 & 3 & \cdots & N \end{array} \\ \begin{bmatrix} m_{11} & m_{12} & 0 & \cdots & 0 \\ m_{21} & m_{22} & m_{23} & 0 & 0 \\ 0 & m_{32} & m_{33} & 0 & 0 \\ \vdots & \vdots & \vdots & \ddots & \vdots \\ 0 & 0 & 0 & \cdots & m_{NN} \end{bmatrix} \end{array}. \tag{12}$$

Here, the proposed similarity transformation method has two important prerequisite conditions: 1) the star-like topology has the same transfer function with the in-line topology, which indicates that they are equivalent in system response, and 2) the coupling matrix of star-like topology is the similar matrix of in-line topology, which indicates that they have the same eigenvalues and can be transformed based on the matrix similarity principle [31], [32]. The key to matrix

similarity transformation lies in determining the rotation pivot and rotation angle, which allows for the gradual elimination of all not-desired cross-coupling resulting from the intermediate stages of the similarity transformation process. For more details, here we introduce the parameters i, j, and k. To eliminate the annihilated element M_{kj} in the coupling matrix of star-like topology, the coupling matrix should be rotated around the pivot $[i, j]$. Afterward, we can obtain the renewed element M_{ki} in the coupling matrix of in-line topology [33]. Simultaneously, the rotation angle used in (11) can be computed as follows:

$$\theta_r = -\tan^{-1}\left(M_{kj}/M_{ki}\right). \tag{13}$$

Continue the aforementioned process iteratively until all the annihilated elements in the coupling matrix of the star-like topology have been converted to the renewed elements in the coupling matrix of the in-line topology. For an N ($N \geqslant 3$) bands MBPFs, it requires total $N_x = (N-1)(N-2)/2$ steps to convert the star-like resonator cell into the in-line resonator cell. For ease of understanding, we will provide a more comprehensive explanation that includes the derivation of the coupling matrix, a detailed list of the parameters involved in the transformation process, the circuit models, and the comparison between the simulated and measured responses in Section III.

III. Synthesis and Design Examples

To validate the similarity transformation method proposed in Section II, three examples of MBPFs, with tri-, quad-, and quint-band prototypes, are synthesized and measured. All three filters are designed as third order and employ a Chebyshev approximation to achieve a passband return loss (RL) of 20 dB. All the designed filters are implemented in the SIW technology, for its high Q-factor, high power capacity, low cost, and high integration, using RT/duroid 5880 substrate (dielectric constant: $\varepsilon_r = 2.2$, height: $h = 0.508$ mm, and dissipation factor: $\tan\delta = 0.0009$) with copper metallization (metal thickness: $t = 17.5$ μm and conductivity: $\sigma = 5.8 \times 10^7$ S.m^{-1}). To protect against copper cladding oxidation and potential performance degradation, all circuits were coated with a protective layer of nickel–gold alloy. Measurements were conducted using a vector network analyzer R&S ZNA, with steps of 1 MHz and the use of through open short match (TOSM) calibration standards.

A. Tri-Band Bandpass Filters

In order to validate the proposed similarity transformation method, the first demonstration is a tri-band BPF. The synthesis process begins with the design of a tri-band prototype using a star-like topology, which allows for the subsequent transformation technique to be applied. The target specifications for the filter are given as follows.

1) *Bandpass 1:* 14.00–14.20 GHz (BW: 200 MHz).
2) *Bandpass 2:* 14.35–14.60 GHz (BW: 250 MHz).
3) *Bandpass 3:* 14.80–15.00 GHz (BW: 200 MHz).

According to the specified bandwidth and RL of target specifications, the design parameters of MBPFs, i.e., the resonant frequencies and slope parameters for each bandpass and bandstop resonators, could be acquired analytically with the generalized frequency method described in [34]. Then, the coupling matrix $M_S^{(3)}$ of star-like resonator cell can be written as follows:

$$M_S^{(3)} = \begin{array}{c} \\ 1 \\ 2 \\ 3 \end{array} \begin{array}{c} \begin{array}{ccc} 1 & 2 & 3 \end{array} \\ \begin{bmatrix} -0.0016 & 0.0235 & 0.0270 \\ 0.0235 & -0.0332 & 0 \\ 0.0270 & 0 & 0.0332 \end{bmatrix} \end{array}. \tag{14}$$

It can be found that all elements on the diagonal of the coupling matrix are not equal to zero, which indicates that the resonator cell is composed of asynchronously coupled circuits, and all the resonators deviate from the center frequency of the passband. Based on this original synthesized star-like coupling matrix, the similarity transformation, as discussed in the theory part, can be exploited to generate the in-line resonator cell. Fig. 4 illustrates the similarity transformation process of tri-band BPF from star-like resonator cell to in-line resonator cell. When $N = 3$, $N_x = 1$. Therefore, there is only one rotation step. The pivot coordinates and the annihilated values involved in the rotation process are listed in Table I.

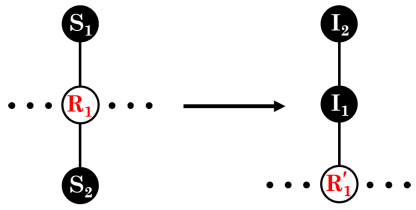

Fig. 4. Similarity transformation of tri-band BPF from star-like resonator cell to in-line resonator cell.

TABLE I
Rotations for Tri-Band Resonator Cell—Star-Like to In-Line

Rotation n^0	Pivot $[i, j]$	Annihilated values	k,j,k,i	θ_r
1	$[2, 3]$	M_{13}	$1, 3, 1, 2$	-0.85441

According to (9)–(12), the coupling matrix $M_I^{(3)}$ of in-line resonator cell can be calculated as (15), and the resonant frequencies can be determined by (6) as: $f_{1'} = \omega_0/2\pi = 14.480$ GHz, $f_{2'} = \omega_1/2\pi = 14.525$ GHz, and $f_{3'} = \omega_2/2\pi = 14.450$ GHz. Due to the periodicity of in-line topology, by further extending the coupling matrix $M_I^{(3)}$ of in-line resonator cell, the complete coupling matrix of the tri-band BPF can be obtained as (16). It is important to note that, in general, the coupling coefficients in the in-line resonator cell tend to be larger than the star-like resonator cell (except $M_{S,13}^{(3)} = 0.0332$ in star-like resonator cell, which is nearly equal to the coupling value $M_{I,2'3'}^{(3)} = 0.0330$ in in-line resonator cell). This characteristic is particularly advantageous for the design of split MBPFs. In the star-like topology, when the filters are set to a specific bandwidth, the bandwidths of the stopbands decrease as the number of passbands increases, resulting in minimal coupling between the bandstop resonators and small coupling coefficients. Therefore, the

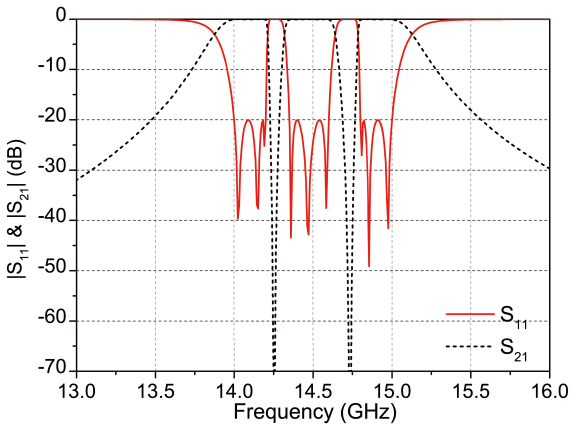

Fig. 5. Theoretical frequency responses of tri-band BPF.

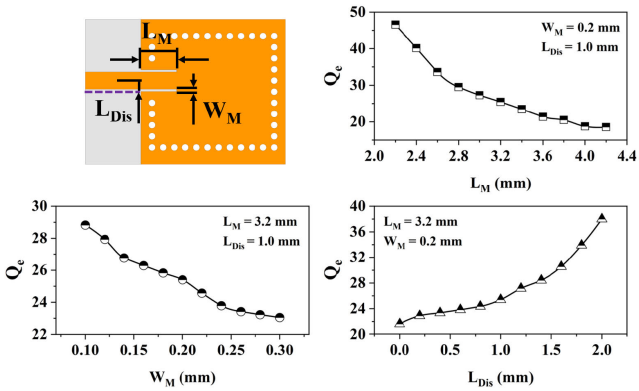

Fig. 6. Variation of Q_e with the length (L_M), the width (W_M), and the offset (L_{Dis}) of coupling slot.

coupling windows become very small, which poses a challenge during the implementation of high-order MBPFs. Fortunately, this challenge can be partially addressed by converting the star-like resonator cell to an in-line resonator cell, which leads to larger coupling coefficients, facilitates the implementation process, especially in high-order MBPFs, and provides greater flexibility and manufacturing tolerance in achieving the desired frequency response. Fig. 5 shows the theoretical simulation frequency response of tri-band BPF. The three simulated bands are in good agreement with the specified requirements

$$M_I^{(3)} = \begin{array}{c} \\ 1' \\ 2' \\ 3' \end{array} \begin{array}{c} \begin{array}{ccc} 1' & 2' & 3' \end{array} \\ \begin{bmatrix} -0.0016 & 0.0358 & 0 \\ 0.0358 & 0.0046 & 0.0330 \\ 0 & 0.0330 & -0.0045 \end{bmatrix} \end{array} \tag{15}$$

$$M_{I\_\mathrm{Tri}} = \begin{array}{c} \\ 1' \\ 2' \\ 3' \\ 4' \\ 5' \\ 6' \\ 7' \\ 8' \\ 9' \end{array} \begin{array}{c} \begin{array}{ccccccccc} 1' & 2' & 3' & 4' & 5' & 6' & 7' & 8' & 9' \end{array} \\ \begin{bmatrix} M_I^{(3)} & & & & & & & & \\ & & & & & & & & \\ & & & M_I^{(3)} & & & & & \\ & & & & & & & & \\ & & & & & & M_I^{(3)} & & \end{bmatrix} \end{array}. \tag{16}$$

Based on the resonant frequencies calculated above, the initial step in developing the electromagnetic (EM) model is identifying the preliminary dimensions of each resonator. Here, we use the SIW square cavity. Disregarding the height, the initial dimensions of each resonator can be determined as follows [35]:

$$f_{\mathrm{T}\,\mathrm{E}_{a0\ b}} = \frac{c}{2\sqrt{\mu_r \varepsilon_r}} \sqrt{\left(\frac{a}{W_{\mathrm{eff}}}\right)^2 + \left(\frac{b}{L_{\mathrm{eff}}}\right)^2} \tag{17}$$

$$W_{\mathrm{eff}} = W - \frac{d^2}{0.95 * p} \tag{18}$$

$$L_{\mathrm{eff}} = L - \frac{d^2}{0.95 * p} \tag{19}$$

where μ_r and ε_r represent the relative permeability and permittivity of substrate, respectively; c denotes the velocity of light in vacuum; a and b correspond to the mode indices; W and L represent the width and length of the cavity, respectively; p is the center-to-center pitch between adjacent via-holes; and d is the diameter of the metalized via-hole. In this work, we only exploit the fundamental TE_{101} mode. The resonant frequency of this mode is directly influenced by the dimensions of the cavity. By precisely controlling the key parameters W and L of the resonators, we can obtain the desired resonant frequencies.

Then, the next step is to determine the dimensions of the coupling slots and coupling windows. The coupling slots are related to the external quality factors (Q_e), defined as follows [36]:

$$Q_e = \frac{f_0}{\Delta f_{\pm 90^\circ}}. \tag{20}$$

Among them, f_0 denotes the resonant frequency corresponding to the peak of S_{11} group delay curve, while $f_{\pm 90^\circ}$ refers to the bandwidth between the deviations of $\pm 90^\circ$ on the S_{11} phase curve. The external quality factors are mainly controlled by the length, the width, and the offset of the coupling slot. Fig. 6 shows the extracted curves of Q_e.

Meanwhile, the coupling windows are related to the internal coupling coefficients. As discussed, the coupling between bandpass resonators is synchronously tuned, while others are asynchronously tuned. Thus, the internal coupling coefficients of synchronous resonators ($M_{ii'}$) and asynchronous resonators ($M_{jj'}$) could be derived using the following equations [37]:

$$M_{ii'} = \frac{f_1^2 - f_2^2}{f_1^2 + f_2^2} \tag{21}$$

$$M_{jj'} = \frac{1}{2}\left(\frac{f_{01}}{f_{02}} + \frac{f_{02}}{f_{01}}\right) \sqrt{\left(\frac{f_1^2 - f_2^2}{f_1^2 + f_2^2}\right)^2 - \left(\frac{f_{01}^2 - f_{02}^2}{f_{01}^2 + f_{02}^2}\right)^2} \tag{22}$$

where f_{01} and f_{02} are self-resonant frequencies of two coupled resonators and f_1 and f_2 are the lower and higher resonant frequencies, respectively. Fig. 7 shows the extracted curves of coupling coefficients.

After calculation and optimization, the EM-simulated model of the designed tri-band BPF is constructed, as shown in Fig. 8. To ensure more accurate simulation results, we also conduct precise modeling and simulation of the spacing 2.92-mm

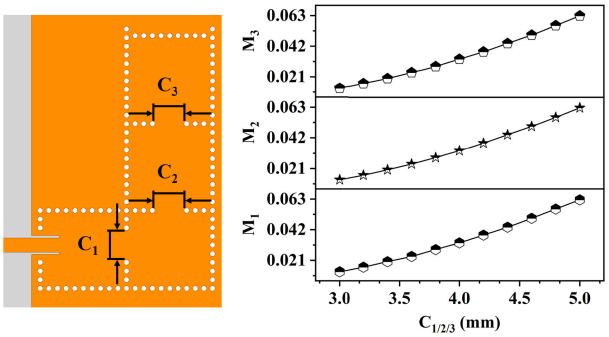

Fig. 7. Variation of internal coupling coefficients with the dimensions of coupling windows.

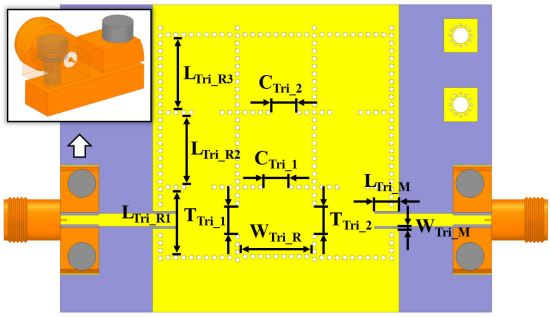

Fig. 8. Dimensional information of tri-band SIW BPF.

TABLE II
DETAILED DIMENSIONS OF TRI-BAND SIW BPF (MM)

L_{Tri_R1}	L_{Tri_R2}	L_{Tri_R3}	T_{Tri_1}	T_{Tri_2}
8.57	9.11	9.53	3.78	3.71
C_{Tri_1}	C_{Tri_2}	W_{Tri_R}	W_{Tri_M}	L_{Tri_M}
3.4	3.4	9.4	0.29	3.19

connector, indicated in the top-left corner of Fig. 8. All key geometrical parameters of the circuit are indicated and reported only once, and the detailed dimensions (in mm) of the tri-band BPF are listed in Table II. The overall size of the prototype circuit is about 34 × 32 mm without considering the 50-Ω microstrip line.

Fig. 9 displays the photograph of the fabricated tri-band BPF. The scattering parameters (magnitude in dB) of filter, both simulated and measured, are shown in Fig. 10 (the wideband frequency responses are measured with a step size of 5 MHz displayed at the bottom). Good agreement between them, especially in terms of TZs and poles, can be observed across the entire frequency band. The first passband is centered at 14.08 GHz with a bandwidth of 220 MHz, the second passband is centered at 14.51 GHz with a bandwidth of 210 MHz, and the third passband is centered at 14.96 GHz with a bandwidth of 260 MHz. A slight frequency shift can be observed, which may be due to dispersion properties, manufacturing tolerances of the substrate, or processing errors of the circuit. From the first to the third passband, the measured minimum insertion loss is 2.55, 2.71, and 2.03 dB. The measured RL is better than 20.32, 22.08, and 19.51 dB. The isolation between the adjacent frequency bands is greater than

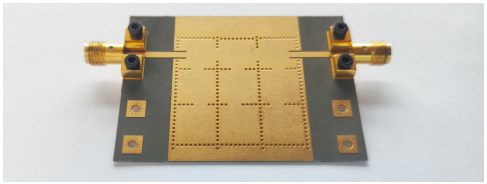

Fig. 9. Photograph of fabricated tri-band SIW BPF.

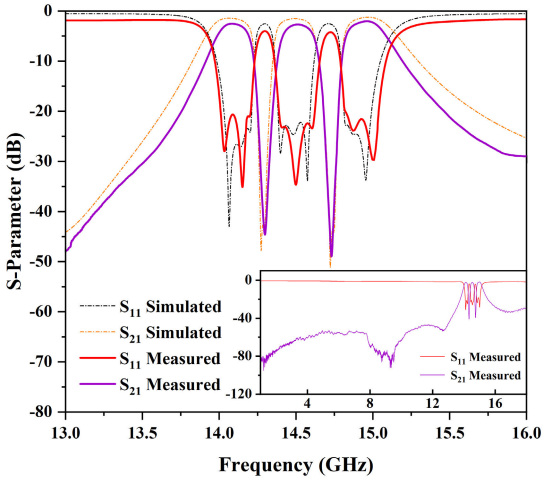

Fig. 10. Simulated and measured results of tri-band SIW BPF.

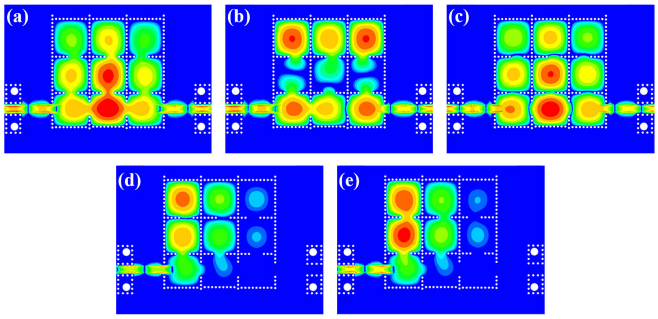

Fig. 11. Electric field distribution in tri-band SIW BPF of (a) 14.10, (b) 14.50, and (c) 14.95 GHz (passband); and (d) 14.25 and (e) 14.72 GHz (stopband).

44.17 and 48.59 dB, respectively. It is worth mentioning that there are multiple TZs in the lower region of the wideband response. The TZs in the first region (8–10 GHz) are generated due to the cutoff frequency of SIW structure, and the TZs in the second region (12–13 GHz) are generated due to the weak cross-coupling between the first and the third resonant cavity in the transverse direction.

Fig. 11 illustrates the electric field magnitude distributions in tri-band SIW BPF of each passband: 14.10, 14.50, and 14.95 GHz, and each stopband: 14.25 and 14.72 GHz. The frequency response in the in-line resonator cell is generated by the excitation of cascade modes, which distinguishes it from multimode resonators. In multimode resonators, multiple resonant modes are excited within a single resonant cavity. However, complex coupling relationships and frequency correlations exist between different modes. As a result, achieving precise and independent control over each mode becomes exceedingly difficult, significantly limiting the flexibility and versatility of frequency design specification in MBPFs and

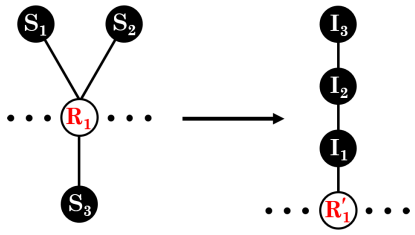

Fig. 12. Similarity transformation of quad-band BPF from star-like resonator cell to in-line resonator cell.

increasing the workload for resonator optimization. In this work, the cascade modes in the resonator cell are excited through the resonator's coupling. All the resonant frequencies can be precisely and independently controlled by adjusting the physical size of each resonator and coupling strength between the adjacent resonators. In this way, the flexibility and versatility of frequency design specifications in MBPFs are significantly enhanced. The theoretical frequency response can be designed rigorously based on the desired performance, providing guidance for filter modeling, and effectively reducing the workload for optimization. This is particularly crucial for the design of complex high-order MBPFs. Furthermore, due to the consistent impedance characteristics and resonant frequencies of the periodic resonator cells in the horizontal direction, the unique TZ between adjacent passbands is actually formed by the overlapping of several TZs equal to the filter order, which effectively enhances the isolation. Disrupting this periodicity, that is, no longer maintaining the consistent resonant frequencies among the resonator cells in the horizontal direction, will result in the splitting of overlapping TZs.

B. Quad-Band Bandpass Filters

In order to further verify the universality of the theory, as a second example, following a similar approach to the tri-band case, the designed quad-band BPF has the following arbitrarily selected passbands.

1) *Bandpass 1:* 13.70–13.88 GHz (BW: 180 MHz).
2) *Bandpass 2:* 14.00–14.14 GHz (BW: 140 MHz).
3) *Bandpass 3:* 14.35–14.50 GHz (BW: 150 MHz).
4) *Bandpass 4:* 14.65–14.85 GHz (BW: 200 MHz).

The corresponding coupling matrix $M_S^{(4)}$ of the quad-band resonator cell can be calculated as follows:

$$M_S^{(4)} = \begin{array}{c} \\ 1 \\ 2 \\ 3 \\ 4 \end{array} \begin{array}{c} \begin{array}{cccc} 1 & 2 & 3 & 4 \end{array} \\ \begin{bmatrix} -0.0005 & 0.0224 & 0.0321 & 0.0249 \\ 0.0224 & -0.0479 & 0 & 0 \\ 0.0321 & 0 & -0.0027 & 0 \\ 0.0249 & 0 & 0 & 0.0456 \end{bmatrix} \end{array}. \tag{23}$$

Fig. 12 illustrates the similarity transformation process of quad-band BPF from star-like resonator cell to in-line resonator cell. When $N = 4$, $N_x = 3$. Therefore, it needs three rotation steps. The pivot coordinates and the annihilated values involved in the rotation process are tabulated in Table III. Then, we can ultimately obtain the coupling matrix $M_I^{(4)}$ of in-line resonator cell, as in (24). They lead to the following resonant frequencies: $f_{1'} = \omega_0/2\pi = 14.260$ GHz, $f_{2'} = \omega_1/2\pi = 14.268$ GHz, $f_{3'} = \omega_2/2\pi = 14.264$ GHz, and $f_{4'} = \omega_2/2\pi = 14.222$ GHz (here, we omit the complete coupling matrix of quad-band BPF). Fig. 13 shows the theoretical frequency response of the quad-band BPF, which matches well with the specified requirements. Fig. 14 exhibits the EM model of the designed quad-band BPF. The detailed dimensions (in mm) are listed in Table IV. The overall size of the circuit is about 42 × 32 mm without considering the 50-Ω microstrip line

TABLE III
ROTATIONS FOR QUAD-BAND RESONATOR CELL—STAR-LIKE TO IN-LINE

Rotation n^0	Pivot $[i, j]$	Annihilated values	k,j,k,i	θ_r
1	$[2, 3]$	M_{13}	$1, 3, 1, 2$	-0.9625
2	$[2, 4]$	M_{14}	$1, 4, 1, 2$	-0.5664
3	$[3, 4]$	M_{24}	$2, 4, 2, 3$	-1.0113

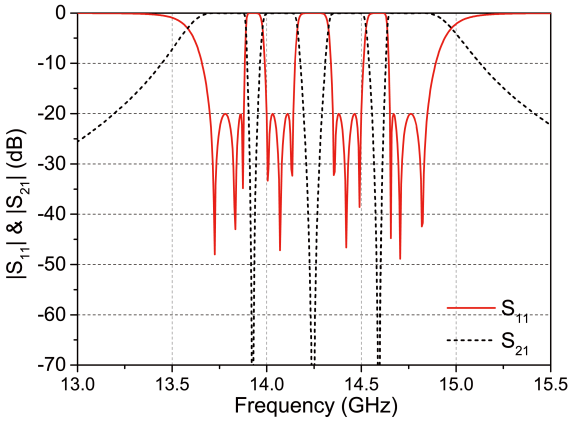

Fig. 13. Theoretical frequency responses of quad-band BPF.

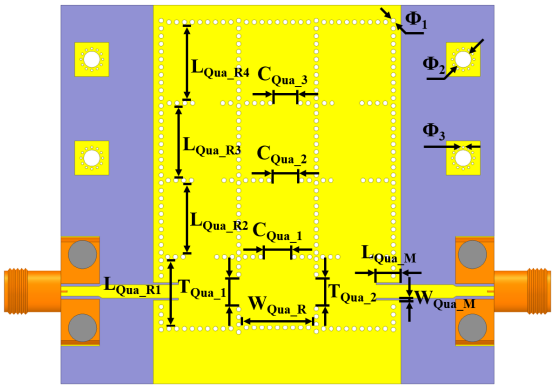

Fig. 14. Dimensional information of quad-band SIW BPF.

$$M_I^{(4)} = \begin{array}{c} \\ 1' \\ 2' \\ 3' \\ 4' \end{array} \begin{array}{c} \begin{array}{cccc} 1' & 2' & 3' & 4' \end{array} \\ \begin{bmatrix} -0.0005 & 0.0464 & 0 & 0 \\ 0.0464 & 0.0007 & 0.0337 & 0 \\ 0 & 0.0337 & 0.0001 & 0.0322 \\ 0 & 0 & 0.0322 & -0.0059 \end{bmatrix} \end{array}. \tag{24}$$

Fig. 15 shows the photograph of the fabricated quad-band BPF. The EM-simulated and measured frequency responses

TABLE IV
DETAILED DIMENSIONS OF QUAD-BAND SIW BPF (MM)

L_{Qua_R1}	L_{Qua_R2}	L_{Qua_R3}	T_{Qua_R4}	T_{Qua_1}
8.73	9.28	9.43	9.85	3.9
T_{Qua_2}	C_{Qua_1}	W_{Qua_2}	C_{Qua_3}	W_{Qua_R}
3.82	3.73	3.6	3.3	9.4
W_{Qua_M}	L_{Qua_M}	Φ_1	Φ_2	Φ_3
0.26	3.23	0.6	2.1	0.3

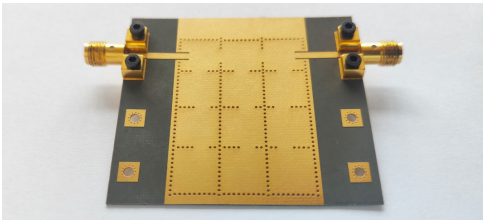

Fig. 15. Photograph of fabricated quad-band SIW BPF.

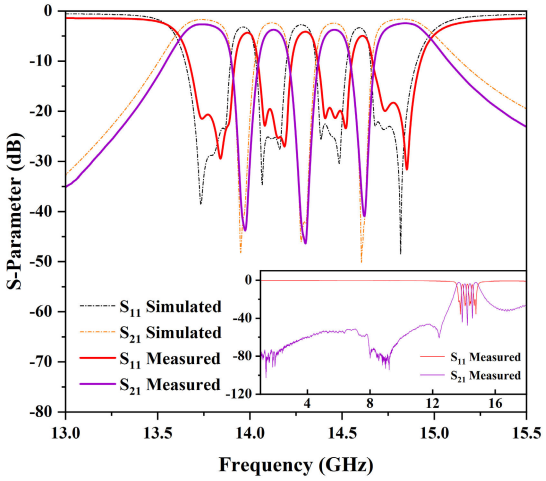

Fig. 16. Simulated and measured results of quad-band SIW BPF.

are shown in Fig. 16. As in the tri-band scenario, the simulated results exhibit good consistency with the measured results in all frequency bands. The first passband is centered at 13.74 GHz with a bandwidth of 240 MHz, the second passband is centered at 14.13 GHz with a bandwidth of 140 MHz, the third passband is centered at 14.46 GHz with a bandwidth of 150 MHz, and the fourth passband is centered at 14.84 GHz with a bandwidth of 270 MHz. From the first to the fourth passband, the measured minimum insertion loss is 2.66, 3.72, 3.74, and 2.43 dB. The measured RL is better than 20.66, 19.58, 19.33, and 18.29 dB. Again, excellent isolation is established between all passbands, greater than 43.74, 46.33, and 40.85 dB between the adjacent frequency bands. Fig. 17 shows the electric field magnitude distributions in quad-band SIW BPF of each passband and stopband.

C. Quint-Band Bandpass Filters

As far as the author knows, there is no reported 3rd order quint-band BPF based on SIW technology in previous

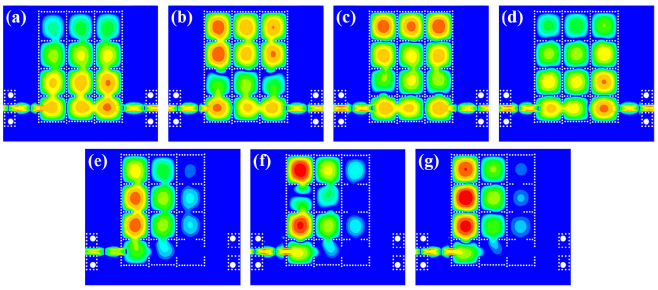

Fig. 17. Electric field distribution in quad-band SIW BPF of (a) 13.80, (b) 14.12, (c) 14.45, and (d) 14.82 GHz (passband); and (e) 13.95, (f) 14.30, and (g) 14.60 GHz (stopband).

work. With the use of the proposed similarity transformation method and in-line topology, the design and implementation of quint-band BPF become feasible.

The arbitrary specifications proposed here to design an example of quint-band BPF are given as follows.

1) *Bandpass 1:* 13.58–13.72 GHz (BW: 140 MHz).
2) *Bandpass 2:* 13.84–14.00 GHz (BW: 160 MHz).
3) *Bandpass 3:* 14.15–14.25 GHz (BW: 100 MHz).
4) *Bandpass 4:* 14.35–14.50 GHz (BW: 150 MHz).
5) *Bandpass 5:* 14.65–14.78 GHz (BW: 130 MHz).

The coupling matrix $M_S^{(5)}$ of the quint-band resonator cell can be written as (25). Fig. 18 illustrates the transformation process. Table V shows the topological rotation parameters, and the coupling matrix $M_I^{(5)}$ of in-line resonator cell can be calculated as (26). They lead to the following resonant frequencies: $f_{1'} = \omega_0/2\pi = 14.150$ GHz, $f_{2'} = \omega_1/2\pi = 14.180$ GHz, $f_{3'} = \omega_2/2\pi = 14.196$ GHz, $f_{4'} = \omega_2/2\pi = 14.139$ GHz, and $f_{5'} = \omega_2/2\pi = 14.218$ GHz. Fig. 19 shows the theoretical frequency responses of quint-band BPF. The five simulated bands are in good agreement with the specifications

$$M_S^{(5)} = \begin{array}{c} \\ 1 \\ 2 \\ 3 \\ 4 \\ 5 \end{array} \begin{array}{c} \begin{array}{ccccc} 1 & 2 & 3 & 4 & 5 \end{array} \\ \begin{bmatrix} -0.0024 & 0.0209 & 0.0268 & 0.0209 & 0.0222 \\ 0.0209 & -0.0591 & 0 & 0 & 0 \\ 0.0268 & 0 & -0.0129 & 0 & 0 \\ 0.0209 & 0 & 0 & 0.0189 & 0 \\ 0.0222 & 0 & 0 & 0 & 0.0618 \end{bmatrix} \end{array} \tag{25}$$

$$M_I^{(5)} = \begin{array}{c} \\ 1' \\ 2' \\ 3' \\ 4' \\ 5' \end{array} \begin{array}{c} \begin{array}{ccccc} 1' & 2' & 3' & 4' & 5' \end{array} \\ \begin{bmatrix} -0.0024 & 0.0457 & 0 & 0 & 0 \\ 0.0457 & 0.0017 & 0.0420 & 0 & 0 \\ 0 & 0.0420 & 0.0040 & 0.0403 & 0 \\ 0 & 0 & 0.0403 & -0.0040 & 0.0222 \\ 0 & 0 & 0 & 0.0222 & 0.0071 \end{bmatrix} \end{array}. \tag{26}$$

To validate this high-order quint-band BPF scheme, the EM model of the designed filter is constructed, as shown in Fig. 20. The detailed dimensions (in mm) are listed in Table VI. The overall size of the circuit is about 54 × 32 mm without considering the 50-Ω microstrip line. Fig. 22 shows the photograph of the fabricated quint-band BPF. Fig. 23 depicts a comparison between simulated and measured curves with good agreement. The first passband is centered at 13.57 GHz with

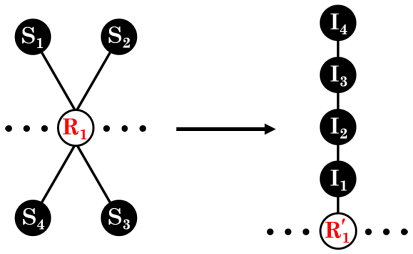

Fig. 18. Similarity transformation of quint-band BPF from star-like resonator cell to in-line resonator cell.

TABLE V
ROTATIONS FOR QUINT-BAND MR CELL—STAR-LIKE TO IN-LINE

Rotation n^0	Pivot $[i, j]$	Annihilated values	k,j,k,i	θ_r
1	$[4, 5]$	M_{15}	$1, 5, 1, 4$	-0.8133
2	$[3, 4]$	M_{14}	$1, 4, 1, 3$	-0.8504
3	$[2, 3]$	M_{13}	$1, 3, 1, 2$	-1.0943
4	$[3, 4]$	M_{24}	$2, 4, 2, 3$	-0.6535
5	$[3, 5]$	M_{25}	$2, 5, 2, 3$	-0.3474
6	$[4, 3]$	M_{35}	$3, 5, 3, 4$	-0.7415

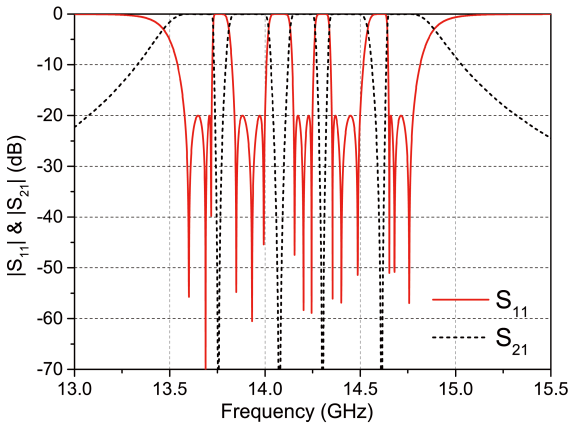

Fig. 19. Theoretical frequency responses of quint-band BPF.

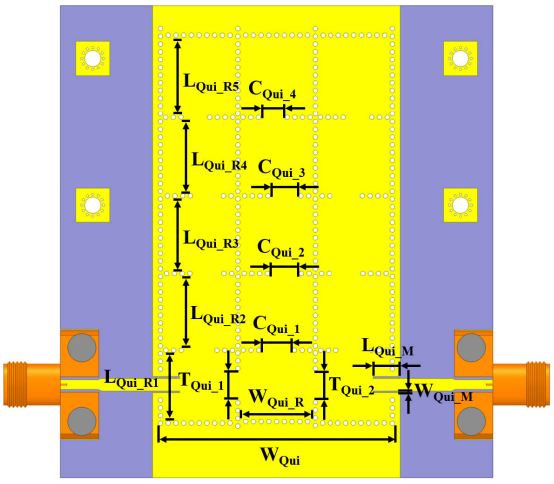

Fig. 20. Dimensional information of quint-band SIW BPF.

a bandwidth of 220 MHz, the second passband is centered at 13.92 GHz with a bandwidth of 100 MHz, the third passband

TABLE VI
DETAILED DIMENSIONS OF QUINT-BAND SIW BPF (MM)

L_{Qui_R1}	L_{Qui_R2}	L_{Qui_R3}	T_{Qui_R4}	T_{Qui_R5}
8.8	9.36	9.42	9.55	10.04
C_{Qui_1}	C_{Qui_2}	C_{Qui_3}	C_{Qui_34}	W_{Qui_R}
4	3.8	3.65	3.09	9.4
T_{Qui_1}	T_{Qui_2}	W_{Qui_M}	L_{Qui_M}	W_{Qui}
3.84	3.77	0.25	3.5	30.6

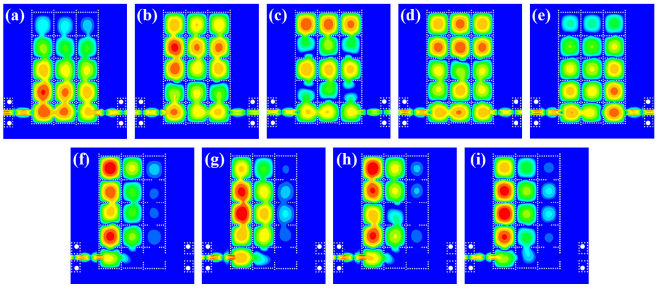

Fig. 21. Electric field distribution in quint-band SIW BPF of (a) 13.60, (b) 13.93, (c) 14.18, (d) 14.45, and (e) 14.76 GHz (passband); and (f) 13.78, (g) 14.05, (h) 14.30, and (i) 14.60 GHz (stopband).

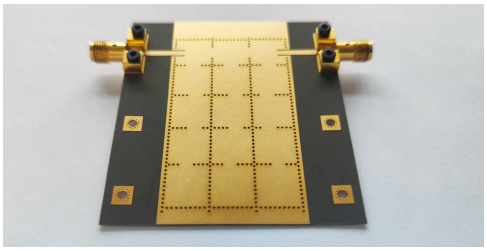

Fig. 22. Photograph of fabricated quint-band SIW BPF.

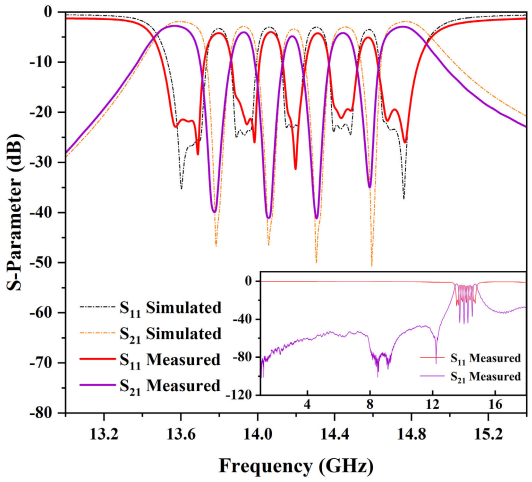

Fig. 23. Simulated and measured results of quint-band SIW BPF.

is centered at 14.18 GHz with a bandwidth of 90 MHz, the fourth passband is centered at 14.45 GHz with a bandwidth of 120 MHz, and the fifth passband is centered at 14.75 GHz with a bandwidth of 210 MHz. From the first to the fifth passband, the measured minimum insertion loss is 2.76, 4.02, 4.85, 4.20, and 2.91 dB, respectively. More insertion loss

TABLE VII
COMPARISONS WITH PREVIOUS WORK OF MBPFS

Refs.	Implemented technology	N_p	Order	CF (GHz)	3-dB FBW(%)	IL (dB)	RL (dB)	Isolation (dB)	Circuirt size ($\lambda_g{}^2$)	Specified bandwidth
[38]	Multi-layer SIW	3	4/2/2	f_1:29.90 f_2:34.80 f_3:36.80	4.33 3.16 3.27	1.65 1.68 1.79	11.13 7.84 9.49	f_1/f_2:43.37 f_2/f_3:20.63	1.35×1.13	No
[20]	Planar SIW	3	3/3/3	f_1:13.00 f_2:14.00 f_3:15.00	4.06 3.31 2.82	1.71 1.80 2.29	16.40 18.80 18.00	f_1/f_2:59.35 f_2/f_3:28.84	3.38×1.19	No
	Planar SIW	3	4/4/4	f_1:11.00 f_2:12.00 f_3:13.00	2.69 1.92 2.25	2.02 2.72 2.57	20.0 18.5 18.5	f_1/f_2:39.25 f_2/f_3:55.92	2.20×2.20	
[39]	Planar SIW	3	3/3/3	f_1:1.11 f_2:1.30 f_3:1.51	6.33 5.41 4.65	0.91 0.89 0.98	7.41 7.26 14.77	f_1/f_2:18.71 f_2/f_3:30.84	0.97×0.48	No
This work	Planar SIW	3	3/3/3	f_1:14.08 f_2:14.51 f_3:14.96	1.56 1.45 1.74	2.55 2.71 2.03	20.32 22.08 19.51	f_1/f_2:44.17 f_2/f_3:48.59	1.64×1.55	Yes
[26]	Multi-layer SIW	4	3/3/3/3	f_1:11.96 f_2:12.96 f_3:13.95 f_4:14.97	2.51 2.55 2.51 1.87	2.26 2.76 2.36 2.88	16.28 12.29 13.82 17.23	f_1/f_2:42.49 f_2/f_3:26.86 f_3/f_4:40.27	1.14×1.08	No
[29]	Planar SIW	4	2/2/2/2	f_1:11.53 f_2:12.51 f_3:14.70 f_4:15.22	1.43 1.42 1.14 1.00	1.33 1.22 1.43 1.53	14.34 20.32 18.89 18.76	f_1/f_2:37.04 f_2/f_3:56.75 f_3/f_4:22.27	2.15×1.27	No
	Planar SIW	4	2/2/2/2	f_1:11.63 f_2:12.47 f_3:13.51 f_4:14.35	1.71 1.68 1.38 1.22	0.89 1.27 1.45 1.36	15.18 16.91 18.64 20.37	f_1/f_2:25.64 f_2/f_3:33.12 f_3/f_4:26.67	1.47×1.06	
This work	Planar SIW	4	3/3/3/3	f_1:13.74 f_2:14.13 f_3:14.46 f_4:14.84	1.75 0.99 1.04 1.82	2.66 3.72 3.74 2.43	20.66 19.58 19.33 18.29	f_1/f_2:43.74 f_2/f_3:46.33 f_3/f_4:40.85	1.99×1.52	Yes
[29]	Planar SIW	5	2/2/2/2/2	f_1:11.57 f_2:11.99 f_3:12.43 f_4:14.21 f_5:14.80	1.46 1.64 1.30 0.98 0.90	0.82 1.10 0.95 1.55 1.74	18.56 18.66 20.81 20.17 17.09	f_1/f_2:17.34 f_2/f_3:15.87 f_3/f_4:50.88 f_3/f_4:24.47	3.08×1.24	No
This work	Planar SIW	5	3/3/3/3/3	f_1:13.57 f_2:13.92 f_3:14.18 f_4:14.45 f_5:14.75	1.62 0.72 0.63 0.83 1.42	2.76 4.02 4.85 4.20 2.91	21.47 16.73 20.16 19.06 19.46	f_1/f_2:39.92 f_2/f_3:41.09 f_3/f_4:41.16 f_3/f_4:34.82	2.56×1.51	Yes

occurs due to the narrow bandwidth of the passband and the relatively lower Q factor of the SIW platform. The measured RL is better than 21.47, 16.73, 20.16, 19.06, and 19.46 dB. The isolation between the adjacent frequency bands is greater than 39.92, 41.09, 41.16, and 34.82 dB. Fig. 21 shows the electric field magnitude distributions in quint-band SIW BPF of each band.

D. Comparisons With Other Reported Works

Table VII presents a comparison between our presented SIW MBPFs (tri-, quad-, and quint-bands) and other previously reported works. Compared to previous studies, the most important contribution of this article is that we propose a systematic, accurate, and flexible theory for MBPF synthesis with in-line topology based on the similarity transformation method. The systematicity is manifested in that throughout all the processes of MBPF synthesis, all the matrix calculation, topology transformation, and model construction processes are guided by detailed and comprehensive theoretical principles and computational formulas. The accuracy is manifested in that the LC parameters extraction process is replaced with the similarity transformation rotation of the coupling matrix, which solves the round-off errors and greatly improves the theoretical accuracy. The flexibility is manifested in that the proposed theory offers flexible control over the frequency responses and the topology structures. In addition, it is also applicable to various platforms such as microstrip lines, SIW, and metal waveguides, allowing for flexible customization to meet specific design requirements.

Apart from the theoretical contributions mentioned above, the designed MBPFs also exhibit several advantages in topology and performance, mainly including simple structure, specified response, and good isolation.

1) *Simple Structure:* Compared to multilayer or other complex planar structures, this article adopts simple in-line topology with periodic structure for MBPF design. The filter order is determined by the number of resonator cells arranged periodically in the horizontal direction,

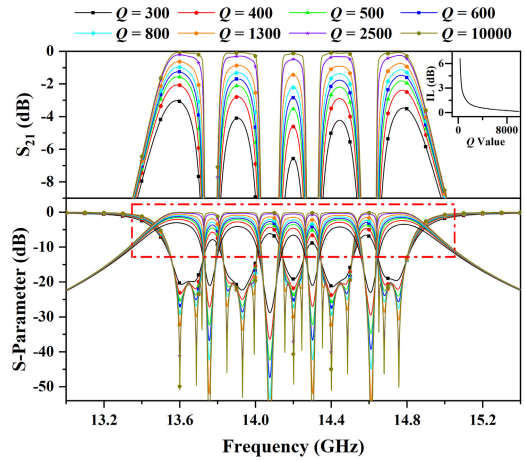

Fig. 24. Simulated frequency response of quint-band SIW BPF with different Q values. (The subfigure in the top-right corner shows the insertion loss of the center frequency band as a function of the Q value.)

while the number of passbands is controlled by the number of stopband resonators arranged in the vertical direction. It effectively simplifies the design complexity and optimization workload of MBPFs, especially in high-order cases, and further reduces the dependence of performance on the manufacturing and assembly process.

2) *Specified Response:* In this work, the similarity transformation method is used to replace the parameter extraction processes, which effectively solves the round-off errors and enables the accurate design of MBPFs at a theoretical level for specific design requirements. Through joint control over the resonant frequencies in the resonator cells, the workload of simulation and optimization for MBPF synthesis can be significantly reduced compared to a multimode structure.
3) *Good Isolation:* In the majority of previous reports, while most frequency bands exhibit good isolation, there are still instances where relatively weak isolation exists between certain adjacent frequency bands. In this work, the unique TZs between adjacent frequency bands are formed by the fusion of several TZs (equal to order), ensuring good isolation among all adjacent frequency bands.

IV. Discussion

A. Loss Mechanism

Based on the proposed similarity transformation method, three examples, including tri-, quad-, and quint-band SIW BPFs, are designed, implemented, and measured. Among them, the discrepancy between simulated and measured insertion loss can primarily be attributed to the deterioration of Q values and the nonlinear attenuation of insertion loss. Fig. 24 illustrates the frequency response of the quint-band SIW BPF for different Q values. As the Q values deteriorate, the insertion loss gradually increases. Notably, this impact is nonlinear, with a more pronounced attenuation as the Q value continuously decreases. The subfigure in the top-right corner shows the insertion loss of the center frequency band as a function of the Q value. For instance, when the Q value of the resonator decreases from 1500 to 1400, the attenuation in insertion loss is 0.05 dB. However, when the Q value decreases from 500 to 400, the attenuation in insertion loss increases to 1.12 dB. Typically, the Q value of SIW resonators falls within the range of 200–800, where the attenuation speed of insertion loss is relatively high. Several factors, including material discontinuities, manufacturing errors, edge effects, and environmental conditions such as temperature and humidity, can contribute to the notable deterioration in the Q values of the fabricated resonators and further exacerbate the attenuation in insertion loss. Fortunately, the proposed similarity transformation method exhibits good universality and is not limited to SIW structures. It can be equally applied to other structures, such as metal waveguides and microstrip lines. By incorporating structures with higher Q values, it is possible to significantly slow down the attenuation of insertion loss, thereby optimizing circuit performance and improving the consistency between simulated and measured results. In addition, the high order, narrowband, and TZs adjacent to the passband in MBPFs are also important factors that influence the insertion loss.

B. Theoretical Flexibility Verification

The similarity transformation method proposed in this article is not limited to the specific cases of narrowband, equal bandwidth, and close band. Instead, it enables flexible design in parameters, such as bandwidth, frequency spacing ratio, filter order, and the number of passbands, which provides a versatile framework for customizing MBPF designs to suit various requirements. To validate this, here we design a seven-order quint-band BPF in theory for the 5G FR1 spectrum, specifically targeting the frequency bands of FR1/n28, n1, n41, n78, and n79. The detailed specifications are outlined as follows.

1) *Bandpass 1 (n28):* 0.70–0.75 GHz (BW: 50 MHz).
2) *Bandpass 2 (n1):* 1.92–1.98 GHz (BW: 60 MHz).
3) *Bandpass 3 (n41):* 2.49–2.69 GHz (BW: 200 MHz).
4) *Bandpass 2 (n78):* 3.30–3.80 GHz (BW: 500 MHz).
5) *Bandpass 3 (n79):* 4.40–5.00 GHz (BW: 600 MHz).

According to (5)–(12), the resonant frequencies can be obtained as: $f_{1'} = 2.603$ GHz, $f_{2'} = 1.252$ GHz, $f_{3'} = 2.785$ GHz, $f_{4'} = 2.932$ GHz, and $f_{5'} = 2.575$ GHz. Fig. 25 illustrates the theoretical frequency responses of the designed seven-order quint-band BPF, demonstrating excellent conformity with the specified requirements. The corresponding variation of conversion loss with Q values are displayed in Fig. 25(b), which exhibits a nonlinear negative correlation. This simulation is primarily used to validate the flexibility of frequency design specification and the accuracy of theoretical coupling matrix calculations of the proposed similarity transformation method at a theoretical level. In practical scenarios, it is necessary to consider the real frequency design specification and the transmission structure characteristics to adjust the actual circuit structure of MBPFs.

C. Topology Rotation Process

The similarity transformation method proposed in this work is based on two prerequisite conditions: the consistency of

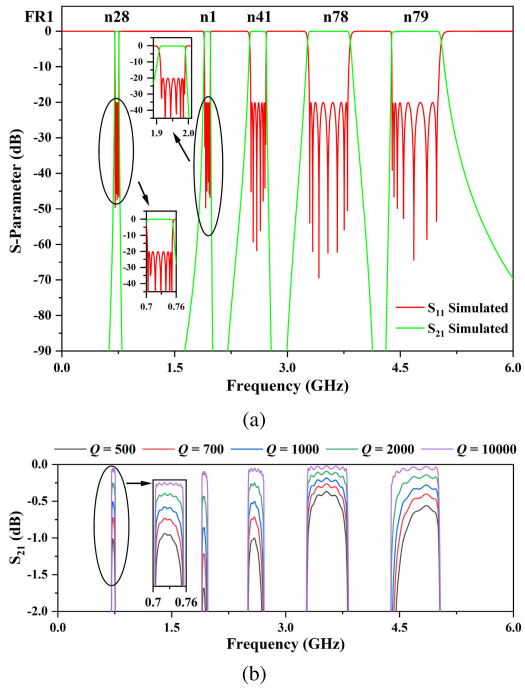

Fig. 25. (a) Theoretical frequency response of a seven-order quint-band BPF. (b) Variation of insertion loss with different Q values.

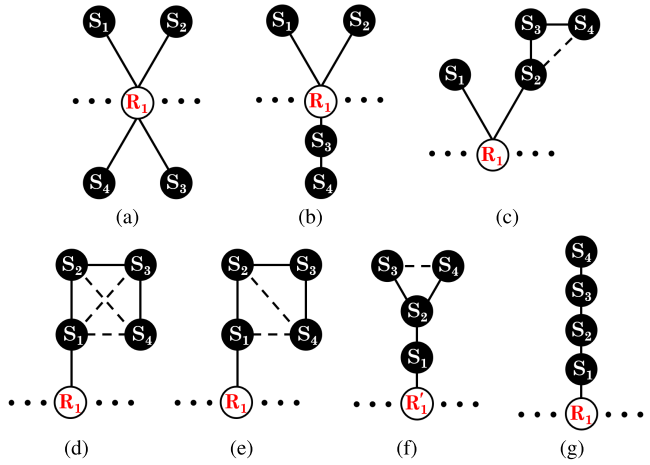

Fig. 26. Intermediate topology structures of the similarity transformation process from star-like topology to in-line topology of the designed quint-band SIW BPF. (a) Star-like topology. (b)–(f) Intermediate topology. (g) In-line topology.

transfer functions and the similarity of coupling matrices between the star-like topology and the in-line topology. With these conditions, the proposed method enables the transformation between the two topology structures while preserving the desired properties of the system. The mathematical essence of the proposed method is the similarity rotation of matrices, while the physical essence is the precise control of couplings between resonators. It is interesting that during the process of similarity transformation, apart from the specific transformation of the topology structure (in this case, the transformation from star-like topology to in-line topology), numerous intermediate states of topology structures are also generated. According to the matrix similarity principle [31], the coupling matrices of these intermediate topology structures have the same eigenvalues and exhibit the same frequency responses, providing a more diverse range of choices for the design of MBPFs in terms of topology structures. For better visualization, we decompose the transformation process of the third-order quint-band MBPFs and provide the diagram of all intermediate topology structures, as shown in Fig. 26. Among them, Fig. 26(a) shows the initial star-like topology, Fig. 26(g) shows the final in-line topology, and Fig. 26(b)–(f) shows the intermediate typologies. Therefore, precise and flexible control of coupling relationships and topology structures is also one of the features in this article.

V. Conclusion

This article introduces a similarity transformation method for converting star-like topology into in-line topology and constructs a general theoretical technique of coupling matrix rotation. Three SIW-based MBPFs, including tri-band, quad-band, and particularly the first reported third-order quint-band, are implemented to validate the proposed method. The experimental results demonstrate good consistency between the simulated and measured frequency responses of MBPFs. The proposed design method significantly enhances the flexibility of high-order MBPF design, particularly enabling precise control over frequency response. Moreover, the theoretical technique has broad applicability in the design of multifrequency devices, such as antennas and multiplexers, satisfying the demands for closely spaced adjacent frequency bands and high level of isolation, holding potential for application in multifrequency wireless communications.

References

[1] K. Wu, M. Bozzi, and N. J. G. Fonseca, "Substrate integrated transmission lines: Review and applications," *IEEE J. Microw.*, vol. 1, no. 1, pp. 345–363, Jan. 2021.

[2] P. Chu et al., "Dual-band substrate integrated waveguide filter with independent TE^{101} and TE^{101} coupling," *IEEE Trans. Microw. Theory Techn.*, vol. 72, no. 3, pp. 1877–1885, Mar. 2024.

[3] F. Zhu, Y. Wu, X. Zhao, P. Chu, G. Q. Luo, and K. Wu, "Compact and wide stopband bandpass filters based on dual-mode folded circular substrate integrated waveguide cavities," *IEEE Trans. Microw. Theory Tech.*vol. 71, no. 7, pp. 3102–3113, Jul. 2023.

[4] K. Zhao and D. Psychogiou, "Monolithic multiband coaxial resonator-based bandpass filter using stereolithography apparatus (SLA) manufacturing," *IEEE Trans. Microw. Theory Techn.*, vol. 70, no. 9, pp. 4156–4166, Sep. 2022.

[5] X.-P. Chen and K. Wu, "Substrate integrated waveguide filters: Design techniques and structure innovations," *IEEE Microw. Mag.*, vol. 15, no. 6, pp. 121–133, Sep. 2014.

[6] C. Roy and K. Wu, "Homotopy optimization and ANN modeling of millimeter-wave SIW cruciform coupler," *IEEE Trans. Microw. Theory Techn.*, vol. 70, no. 11, pp. 4751–4764, Nov. 2022.

[7] J. L. Gómez-Tornero, A. J. Martínez-Ros, S. Mercader-Pellicer, and G. Goussetis, "Simple broadband quasi-optical spatial multiplexer in substrate integrated technology," *IEEE Trans. Microw. Theory Techn.*, vol. 63, no. 5, pp. 1609–1620, May 2015.

[8] S. Yan, P. J. Soh, and G. A. E. Vandenbosch, "Dual-band textile MIMO antenna based on substrate-integrated waveguide (SIW) technology," *IEEE Trans. Antennas Propag.*, vol. 63, no. 11, pp. 4640–4647, Nov. 2015.

[9] J. W. Holloway, G. C. Dogiamis, S. Shin, and R. Han, "220-to-330-GHz manifold triplexer with wide stopband utilizing ridged substrate integrated waveguides," *IEEE Trans. Microw. Theory Techn.*, vol. 68, no. 8, pp. 3428–3438, Aug. 2020.

[10] Y. Dong, C.-T.-M. Wu, and T. Itoh, "Miniaturised multi-band substrate integrated waveguide filters using complementary split-ring resonators," *IET Microw., Antennas Propag.*, vol. 6, no. 6, pp. 611–620, Apr. 2012.

[11] X.-P. Chen and K. Wu, "Self-packaged millimeter-wave substrate integrated waveguide filter with asymmetric frequency response," *IEEE Trans. Compon., Packag., Manuf. Technol.*, vol. 2, no. 5, pp. 775–782, May 2012.

[12] D. Zhao, F. Lin, Z. Zhai, H. Sun, and X. Y. Zhang, "Design of nonreciprocal filtering antenna using spatio-temporal modulated SIW resonators," *IEEE Trans. Microw. Theory Techn.*, vol. 71, no. 10, pp. 4505–4518, Oct. 2023.

[13] S. I. Shams, S. M. Sifat, M. Elsaadany, G. Gagnon, and A. A. Kishk, "Systematic design procedure for Y-junction circulator based on ridge gap waveguide technology," *IEEE Trans. Microw. Theory Techn.*, vol. 69, no. 4, pp. 2165–2177, Apr. 2021.

[14] Y. Zhu and Y. Dong, "A compact dual-band quasi-elliptic filter based on hybrid SIW and microstrip technologies," *IEEE Trans. Circuits Syst. II, Exp. Briefs*, vol. 69, no. 3, pp. 719–723, Mar. 2022.

[15] X. Zhou, G. Zhang, J. Zheng, W. Tang, and J. Yang, "SIW filter with adjustable number of passbands using assembled multimode resonant PCBs," *IEEE Trans. Circuits Syst. II, Exp. Briefs*, vol. 69, no. 8, pp. 3386–3389, Aug. 2022.

[16] D. Li, W. Luo, X. Chen, Y. Liu, K.-D. Xu, and Q. Chen, "Miniaturized dual-/tri-/quad-band bandpass filters using perturbed multimode SIW cavity," *IEEE Trans. Compon., Packag., Manuf. Technol.*, vol. 13, no. 10, pp. 1685–1693, Oct. 2023.

[17] K. Zhou and K. Wu, "Multichannel substrate integrated waveguide diplexers based on orthogonal dual modes and split-type multiband responses," *IEEE Trans. Microw. Theory Techn.*, vol. 70, no. 1, pp. 356–366, Jan. 2022.

[18] D. Li, X. Chen, W. Luo, Z. Zheng, and Q. Chen, "Compact tri-band SIW bandpass filters with high selectivity and controllable center frequencies using perturbation structure," *IEEE Trans. Circuits Syst. II, Exp. Briefs*, vol. 70, no. 11, pp. 4043–4047, Nov. 2023.

[19] K. Zhou, C.-X. Zhou, and W. Wu, "Substrate-integrated waveguide dual-band filters with closely spaced passbands and flexibly allocated bandwidths," *IEEE Trans. Compon., Packag., Manuf. Technol.*, vol. 8, no. 3, pp. 465–472, Mar. 2018.

[20] H. Xie, K. Zhou, C. Zhou, and W. Wu, "Substrate-integrated waveguide triple-band bandpass filters using triple-mode cavities," *IEEE Trans. Microw. Theory Techn.*, vol. 66, no. 6, pp. 2967–2977, Jun. 2018.

[21] K. Zhou, C.-X. Zhou, and W. Wu, "Resonance characteristics of substrate-integrated rectangular cavity and their applications to dual-band and wide-stopband bandpass filters design," *IEEE Trans. Microw. Theory Techn.*, vol. 65, no. 5, pp. 1511–1524, May 2017.

[22] X. Zhou et al., "Design of 3-D integrated SIW multiband bandpass filter with split-type extended doublet topology," *IEEE Trans. Compon., Packag., Manuf. Technol.*, vol. 12, no. 10, pp. 1681–1691, Oct. 2022.

[23] B.-J. Chen, T.-M. Shen, and R.-B. Wu, "Dual-band vertically stacked laminated waveguide filter design in LTCC technology," *IEEE Trans. Microw. Theory Techn.*, vol. 57, no. 6, pp. 1554–1562, Jun. 2009.

[24] M.-H. Ho and K.-H. Tang, "Miniaturized SIW cavity tri-band filter design," *IEEE Microw. Wireless Compon. Lett.*, vol. 30, no. 6, pp. 589–592, Jun. 2020.

[25] K.-S. Chin, C.-C. Chang, C.-H. Chen, Z. Guo, D. Wang, and W. Che, "LTCC multilayered substrate-integrated waveguide filter with enhanced frequency selectivity for system-in-package applications," *IEEE Trans. Compon., Packag., Manuf. Technol.*, vol. 4, no. 4, pp. 664–672, Apr. 2014.

[26] X. Guo, L. Zhu, and W. Wu, "Design method for multiband filters with compact configuration in substrate integrated waveguide," *IEEE Trans. Microw. Theory Techn.*, vol. 66, no. 6, pp. 3011–3018, Jun. 2018.

[27] X.-P. Chen, K. Wu, and Z.-L. Li, "Dual-band and triple-band substrate integrated waveguide filters with Chebyshev and quasi-elliptic responses," *IEEE Trans. Microw. Theory Techn.*, vol. 55, no. 12, pp. 2569–2578, Dec. 2007.

[28] M. Esmaeili and J. Bornemann, "Substrate integrated waveguide triple-passband dual-stopband filter using six cascaded singlets," *IEEE Microw. Wireless Compon. Lett.*, vol. 24, no. 7, pp. 439–441, Jul. 2014.

[29] K. Zhou, C.-X. Zhou, H.-W. Xie, and W. Wu, "Synthesis design of SIW multiband bandpass filters based on dual-mode resonances and split-type dual- and triple-band responses," *IEEE Trans. Microw. Theory Techn.*, vol. 67, no. 1, pp. 151–161, Jan. 2019.

[30] H. Di, B. Wu, X. Lai, and C.-H. Liang, "Synthesis of cross-coupled triple-passband filters based on frequency transformation," *IEEE Microw. Wireless Compon. Lett.*, vol. 20, no. 8, pp. 432–434, Aug. 2010.

[31] F. Zhang, *Matrix Theory: Basic Results and Techniques*. Springer, 2011.

[32] P. Ma, B. Wei, J. Hong, X. Guo, B. Cao, and L. Jiang, "Coupling matrix compression technique for high-isolation dual-mode dual-band filters," *IEEE Trans. Microw. Theory Techn.*, vol. 66, no. 6, pp. 2814–2821, Jun. 2018.

[33] R. J. Cameron, C. M. Kudsia, and R. R. Mansour, *Microwave Filters for Communication Systems: Fundamentals, Design, and Applications*. Hoboken, NJ, USA: Wiley, 2018.

[34] Y. Wu, E. Fourn, P. Besnier, and C. Quendo, "Direct synthesis of multiband bandpass filters with generalized frequency transformation methods," *IEEE Trans. Microw. Theory Techn.*, vol. 69, no. 8, pp. 3820–3831, Aug. 2021.

[35] X. Wang, X. Zhu, Z. H. Jiang, Z. Hao, Y. Wu, and W. Hong, "Analysis of eighth-mode substrate-integrated waveguide cavity and flexible filter design," *IEEE Trans. Microw. Theory Techn.*, vol. 67, no. 7, pp. 2701–2712, Jul. 2019.

[36] S. W. Wong, K. Wang, Z.-N. Chen, and Q.-X. Chu, "Design of millimeter-wave bandpass filter using electric coupling of substrate integrated waveguide (SIW)," *IEEE Microw. Wireless Compon. Lett.*, vol. 24, no. 1, pp. 26–28, Jan. 2014.

[37] J.-S. G. Hong and M. J. Lancaster, *Microstrip Filters for RF/Microwave Applications*. Hoboken, NJ, USA: Wiley, 2004.

[38] W.-L. Tsai, T.-M. Shen, B.-J. Chen, T.-Y. Huang, and R.-B. Wu, "Triband filter design using laminated waveguide cavity in LTCC," *IEEE Trans. Compon., Packag., Manuf. Technol.*, vol. 4, no. 6, pp. 957–966, Jun. 2014.

[39] S. A. Shakib, V. Sekar, and K. Entesari, "A compact triple-band bandpass filter based on half-mode substrate integrated waveguides," in *Proc. 42nd Eur. Microw. Conf.*, Oct. 2012, pp. 116–119.

Yu Zhan (Student Member, IEEE) received the B.E. degree from Tianjin University, Tianjin, China, in 2022, where he is currently pursuing the Ph.D. degree.

His current research interests include the design of terahertz front-end systems, RF filters, and power amplifiers for communication applications.

Mr. Zhan was a recipient of China Youth Science and Technology Innovation Award, which is known as the highest award for youth science and technology innovation in China.

Yi Wu (Member, IEEE) was born in Tai'an, Shandong, China. He received the Ph.D. degree from the Institut National des Sciences Appliquées de Rennes (INSA-Rennes), Rennes, France, in July 2021.

Since 2021, he has been a Post-Doctoral Researcher at the School of Microelectronics, Tianjin University, Tianjin, China. He has authored or coauthored over 20 journal articles and international conference papers. His recent research interests are mainly in the design of microwave components, especially microwave passive filters.

Dr. Wu has served as a reviewer for IEEE TRANSACTIONS ON MICROWAVE THEORY AND TECHNIQUES, IEEE TRANSACTIONS ON CIRCUITS AND SYSTEMS—I: REGULAR PAPERS, *IET Microwave Antennas and Propagation*, and other IEEE papers and conferences.

Erwan Fourn (Member, IEEE) received the M.S. and Ph.D. degrees in electronics from the University of Brest, Brest, France, in 2001 and 2004, respectively.

He was a Post-Doctoral Fellow at LAAS-CNRS, Toulouse, France. Since 2006, he has been an Associate Professor with the National Institute of Applied Sciences (INSA), Rennes, France. Through different projects on reconfigurable antennas and circuits, he studied and used different reconfiguration solutions (MEMS, p-i-n diodes, ferroelectric materials, VO_2, chalcogenide materials, and so on). He is a supervisor and a director of several Ph.D. theses and a coordinator of some research bilateral or multipartner projects. His research activities, within the the Institut d'Electronique et des Technologies du numéRique (IETR), INSA, are mainly focused on the design of passive and reconfigurable reflect- and transmit-array antennas and filters for microwave and millimeter-wave applications.

Philippe Besnier (Senior Member, IEEE) received the Diplôme d'ingénieur degree in electronics from the École universitaire d'ingénieurs de Lille (EUDIL), Lille, France, in 1990, and the Ph.D. degree in electronics from the University of Lille, Lille, in 1993.

Following a one-year period at ONERA, Palaiseau, France, as an Assistant Scientist at the IEEE TRANSACTIONS ON ELECTROMAGNETIC COMPATIBILITY (EMC) Division, he was with the Laboratory of Radio-Propagation and Electronics (LRPE), University of Lille, as a Researcher (chargé de recherche) at the Centre National de la Recherche Scientifique (CNRS) from 1994 to 1997. From 1997 to 2002, he was the Director of the Centre d'Etudes et de Recherches en Protection Electromagnétique (CERPEM), Laval, France: a not-for-profit organization for research, expertise, and training in EMC and related activities. He co-founded and headed TEKCEM, Laval, in 1998, a small business company specialized in turn-key systems for EMC measurements. Since 2002, he has been with the Institut d'Electronique et des Technologies du numéRique (IETR), Rennes, France. He was appointed as a CNRS Senior Researcher (directeur de recherche au CNRS) in 2013. He was the Co-Head of the Antennas and Microwave Devices Research Department, IETR, from 2012 to 2016. He headed the WAVES (now eWAVES) Team—electromagnetic waves in complex media—during the first semester of 2017. Since July 2017, he has been the Deputy Director of the IETR. His research activities deal with interference analysis on cable harnesses (including electromagnetic topology), theory and application of reverberation chambers, shielding and absorbing techniques, quantification and propagation of uncertainties in EMC modeling, and electromagnetic cybersecurity.

Kaixue Ma (Fellow, IEEE) received the B.E. and M.E. degrees from Northwestern Polytechnical University (NWPU), Xi'an, China, in 1997 and 2002, respectively, and the Ph.D. degree from Nanyang Technological University (NTU), Singapore, in 2007.

From 1997 to 2002, he worked at Chinese Academy of Space Technology, Xi'an, as a Group Leader. From 2005 to 2007, he was with MEDs Technologies as a Research and Development Manager. From 2007 to 2010, he was with ST Electronics as a Research and Development Manager and a Project Leader. He was a Technique Management Committee and Technique Consultant in 2011. From 2010 to 2013, he was with NTU as a Senior Research Fellow and a Millimeter-Wave RFIC Team Leader for the 60-GHz Flagship Chipset Project. From 2013 to 2018, he was a Full Professor with the University of Electronic Science and Technology of China (UESTC), Chengdu, China. Since February 2018, he has been the Dean and a Distinguished Professor with the School of Microelectronics, Tianjin University, Tianjin, China; a Principal Investigator of the National IC Innovation and Entrepreneurship Platform of Tianjin; and the Director of Tianjin Key Laboratory of Imaging and Sensing Microelectronics Technology. He proposed a variety of RF and microwave integrated circuits based on advanced CMOS, SiGe BiCMOS, GaAs, and CMOS silicon-on-insulator (SOI) technologies, and microwave circuit and system design technology patented with "quasi-planar circuits with embedded air cavity" named as SISL in publication. The preliminary research and development results were partially transformed into the company's flagship products sold to Europe and USA or used in China's on-orbit satellites. He was responsible for designing and implementing the first low-power reconfigurable 60-GHz SiGe millimeter-wave transceiver system-on-chip (SOC), packaging, and system testing, and completed a high-speed dual-chip wireless communication system. The results were reported by dozens of technology media. He has filed over 50 patents and published three books and over 400 science citation index/engineering index (SCI/EI) indexed articles in the fields of RF/microwave, millimeter-wave, and THz-integrated circuits and systems, including over 200 IEEE journal articles and over 200 IEEE conference papers.

Dr. Ma is a Fellow of Chinese Institute of Electronics and an Awardee of Chinese National Science Fund for Distinguished Young Scholar. He received ten technique awards, including the Best Paper Award, and the Emerging Technology Awards from Singapore Information and Communication Technology Association. He has been the Chairperson of Tianjin IC Association. He was Associate Editor of IEEE TRANSACTIONS ON MICROWAVE THEORY AND TECHNIQUES and a Guest Editor of *IEEE Microwave Magazine*. He is an organizer for international conferences. He was the Coordinator of IEEE MTT-S R10 for China and Singapore from 2016 to 2022 and is a member of MTT-S TC-4.